Alignment of the aberration-free XUV Raman spectrometer at FLASH

Mykola Biednov,[a,b]* Günter Brenner,[c] Benjamin Dicke,[a,b] Holger Weigelt,[c] Barbara Keitel,[c] Michael Rübhausen[a,b] and Siarhei Dziarzhytski[c]

[a]Institut für Nanostruktur- und Festkörperphysik, Universität Hamburg, Notkestrasse 85, Hamburg, 22607, Germany, [b]Center for Free-Electron Laser Science, Deutsches Elektronen-Synchrotron, Notkestrasse 85, Hamburg, 22607, Germany, and [c]Deutsches Elektronen-Synchrotron DESY, Notkestrasse 85, Hamburg, 22607, Germany. *Correspondence e-mail: mbiednov@physnet.uni-hamburg.de

An extreme-ultraviolet (XUV) double-stage Raman spectrometer is permanently installed as an experimental end-station at the PG1 beamline of the soft X-ray/XUV free-electron laser in Hamburg, FLASH. The monochromator stages are designed according to the Czerny–Turner optical scheme, adapted for the XUV photon energy range, with optical elements installed at grazing-incidence angles. Such an optical scheme along with the usage of off-axis parabolic mirrors for light collimation and focusing allows for aberration-free spectral imaging on the optical axis. Combining the two monochromators in additive dispersion mode allows for reaching high resolution and superior stray light rejection, but puts high demands on the quality of the optical alignment. In order to align the instrument with the highest precision and to quantitatively characterize the instrument performance and thus the quality of the alignment, optical laser interferometry, Hartmann–Shack wavefront-sensing measurements as well as off-line soft X-ray measurements and extensive optical simulations were conducted. In this paper the concept of the alignment scheme and the procedure of the internal optical alignment are presented. Furthermore, results on the imaging quality and resolution of the first monochromator stage are shown.

1. Introduction

Resonant inelastic X-ray light scattering (RIXS) is a powerful spectroscopic tool that can be utilized to study different types of elementary excitations in, for example, strongly correlated systems like manganites or cuprates, or charge transfer processes in bio-inorganic molecules with metal centers (Ament et al., 2011; Rusydi et al., 2014). RIXS is a photon-in/photon-out process in which the change in the energy and momentum of the incident photon during the scattering process is investigated. The technique is element- and orbital-specific when it is in resonance with an atomic absorption edge by inducing specific orbital transitions of the element of interest. At the same time, such a tuning of the incident energy may result in a great enhancement of the scattering cross section due to the resonant nature of the scattering process (Kotani & Shin, 2001). RIXS is a 'photon hungry' technique and the availability of tunable high-brilliance sources is crucial for an experiment. Moreover, growing interest in dynamics studied via RIXS requires short in femtosecond-to-picosecond range excitation pulses which nowadays are more available at free-electron laser (FEL) light sources. The high-brilliance high-repetition-rate free-electron laser FLASH is capable of providing sub-100 fs pulses with the wavelength in the range 4.2–51 nm (Ackermann et al., 2007), which covers the range of

L-edges of lighter elements or *M*-edges of the heavier ones, such as transition metals, and *N*-edges of rare-earth elements. These properties were decisive in building an XUV Raman spectrometer as a permanent end-station.

From an experimental point of view, the successful realization of RIXS experiments puts high demands on the instrument, especially when low-energy excitations with typically sub-50 meV excitation energies are studied and interaction cross-sections are small. To meet this purpose, a two-stage double-monochromator Raman spectrometer with an intermediate slit was designed (Rusydi *et al.*, 2014; Rübhausen *et al.*, 2004). Each spectrometer stage works according to the Czerny–Turner optical scheme and enables aberration-free spectral imaging on the optical axis. In order to achieve superior resolution and stray light rejection, the design also requires special care in the alignment of the instrument. One of the most crucial aspects of the confocal operation mode with an intermediate slit is that the position of the intermediate focal plane must remain fixed for all photon energies or consequently for all possible angles of the diffraction grating. Therefore, three different techniques were combined in order to align the optical components and verify their aligned state. As the main alignment technique, optical laser interferometry was employed. It allows evaluation of the quality of the laser wavefront behind different optical elements of the monochromator with a precision of the order of the wavelength of light used (here 633 nm). Complementarily, wavefront sensing using a Hartmann–Shack wave-

front sensor (LOT, https://lot-qd.de/de/produkte/licht-laser/laser-beam-diagnostics/product/hartmann-shack-wellenfront sensor-1/; Schäfer *et al.*, 2006) was used and the results obtained were cross-checked with those from the optical laser interferometry studies. Finally, the alignment quality of the monochromator was validated by employing an off-line X-ray source, which has been adapted to provide soft X-ray photons. This could be used to perform systematic performance tests in the energy region of interest and independent of the FEL availability.

2. XUV Raman spectrometer overview

The high-resolution double-stage XUV Raman spectrometer is a permanent end-station of the PG1 branch of the plane-grating monochromator beamline at FLASH (Martins *et al.*, 2006; Dziarzhytski *et al.*, 2016; Tiedtke *et al.*, 2009). This instrument has been developed at the University of Hamburg in collaboration with DESY for inelastic scattering (Raman) experiments in the soft X-ray spectral region from 20 to 200 eV, intended to provide high spectral resolution of 2–15 meV and superior stray light suppression, which allows studies of low-energy quasiparticles in various solid samples. The spectrometer design is based on a confocal additive arrangement of two high-resolution monochromator stages, shown in Fig. 1 (Rusydi *et al.*, 2014; Rübhausen *et al.*, 2004). In brief, the sample is located in the sample chamber and emits under illumination with the FEL radiation elastically and
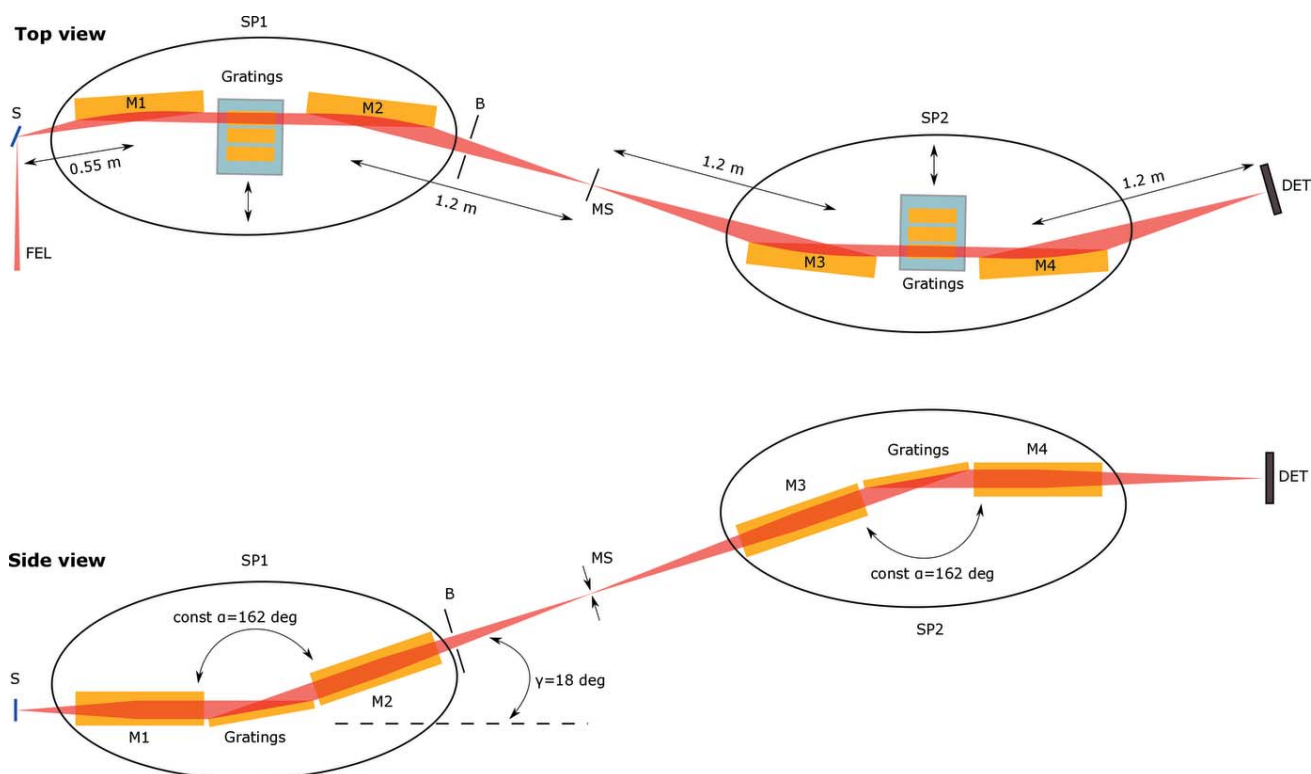

Figure 1
Optical scheme of the XUV Raman spectrometer. M1–M4: off-axis parabolic mirrors; MS: middle slit: B: baffle system; S: sample; DET: detector camera; SP1, SP2: monochromator chambers.

inelastically scattered photons. Both types of photons are collected by the first monochromator stage. This stage also acts effectively as an entrance objective that collects a relatively large solid angle (v × h = 37 mrad × 82.6 mrad) and reduces the stray light by predispersing the light separating the elastic from the inelastic contribution. A slit mechanism situated between the monochromators allows only photons into the second stage that are inelastically scattered. The second stage is the spectrograph stage that disperses the light further onto the detector plane, where the spectrum is recorded by an intensified charge-coupled camera (ICCD). Each monochromator chamber, shown in Fig. 1 as SP1 and SP2, houses two off-axis parabolic mirrors for light collimation and focusing and a grating bench that can hold up to four optical gratings. The schematic layout of the monochromator is depicted in Fig. 1.

The sample S is located in the focal point of the first off-axis parabolic (OAP) mirror M1. The scattered light is collimated and directed onto the grating unit G1. Note that in both monochromator stages the parabolic mirrors deflect the beam perpendicular to the dispersion plane. Thus, the light is focused along the short axis of the parabola (sagittal focusing), reducing the influence of optic slope errors. The maximum acceptance angle of M1 is 37 mrad × 82.6 mrad (v × h). G1 works in inside order orientation. The vertically dispersed photons are collected and focused onto the intermediate slit (labeled MS in Fig. 1) by the second OAP mirror M2. As mentioned before, the light transmitted through the intermediate slit is then collected and further dispersed by the second monochromator stage in a similar fashion. The Raman spectrometer works with a constant included angle of $162°$, thus the mirror positions are fixed; only the gratings have to be rotated in order to choose or scan the wavelength, enabling the operation as a double monochromator. By using the gratings in zeroth order, any wavelength can be focused. This property is used in the alignment process of the instrument.

The grating unit G1 of the first monochromator stage hosts two plane diffraction gratings, G1-3 and G1-4, with groove densities of 576 lines mm^{-1} and 1120 lines mm^{-1}, covering the spectral energy ranges of 36–144 eV and 70–210 eV, respectively. Gratings are switched between each other by moving them transversely to the beam in the horizontal plane (see Fig. 1). In addition, a plane mirror is installed and can be used instead of the diffraction grating in case a higher throughput is needed.

3. Alignment

In this section we present the procedure and the results of the internal optical alignment of the single XUV Raman monochromator SP1. The optical alignment approach was based on using a Laser Unequal Path Interferometer (LUPI) from Space Optics Research Labs, coupled with a 90° off-axis focusing parabolic mirror (FP), to provide a source point for the XUV Raman monochromator (see Fig. 2). A single-mode He–Ne laser with central wavelength of 633 nm is used to provide the laser beam for the interferometric alignment. LUPI and FP were mounted as one unit on a common laser breadboard, installed on a hexapod from Physik Instrumente (PI, model number H-850.H2). This allowed precise control over the source point position and its fine-tuning. Complementarily, the evaluation of the alignment quality was performed via wavefront-sensing measurements (Keitel et al., 2016).

The alignment procedure consists of four major steps that will be further discussed in the following:

(1) Alignment of the FP.

(2) Alignment of the LUPI stage with respect to the OAP mirror M1.

(3) Alignment of the gratings at unit G1 (one by one).

(4) Alignment of the OAP mirror M2.

3.1. Interferometer preparation

At a first alignment step, the laser beam in the test arm of the LUPI spectrometer has to be focused to create a source point for the first mirror M1 of the XUV Raman spectrometer. Considering the numerical aperture of the OAP mirror M1 and the need to fold the laser beam due to space constraints in the FLASH experimental hall, a 90° OAP mirror with parental focal distance of 75 mm was used. The surface quality of this OAP mirror is $\lambda/4$. The mirror is 1 inch in diameter, which
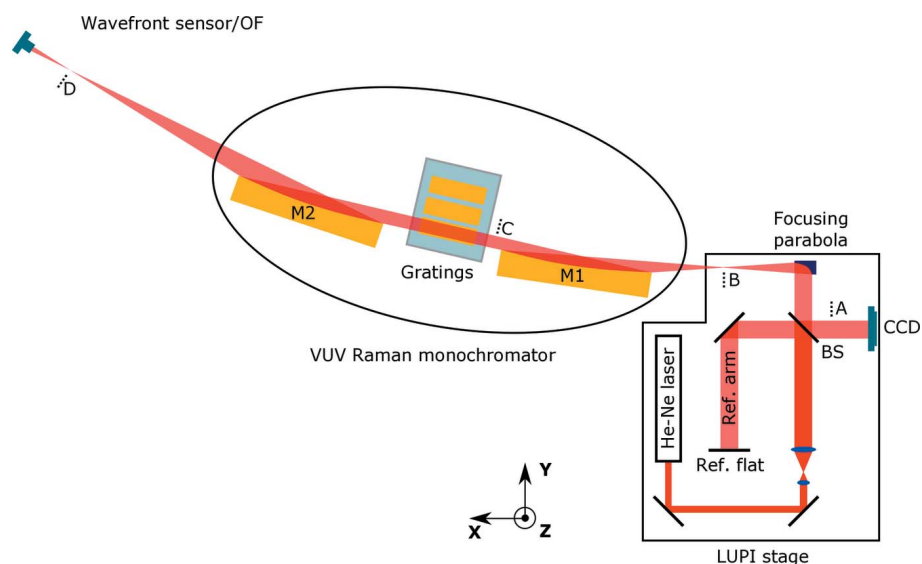

Figure 2
Optical scheme of the LUPI stage, coupled to the XUV Raman monochromator chamber. The beamsplitter (BS) splits the beam from the single-mode He–Ne laser into reference and test arms and recombines them again on the CCD. The beam in the test arm is focused by the FP to create a source point for the M1 mirror of the monochromator. During different stages of the alignment process, the optical flat mirror (OF) has to be placed at points B, C and D. An imaging lens can be placed at position A for pre-alignment purposes. A retro-reflector was used at position C as explained in Section 3.2.

corresponds to an f-number of 5.91. The smaller f-number of the focusing parabola compared with that of M1 means that the mirror M1 is over-illuminated by the FP. Thus only the central part of the wavefront with the highest quality, provided by the FP, will illuminate M1 and participate in the formation of the interference pattern. The FP is placed in a kinematic mount which allows pitch, roll and yaw adjustments. The alignment was performed according to the scheme depicted in Fig. 2. A high-quality ($\lambda/20$) optical flat mirror (OF) was placed in the focal point of the FP (position B) and the pairs of degrees of freedom pitch/yaw of the focusing parabola and tip/tilt of the OF were altered together to achieve parallel and uniformly distributed fringes in the interferogram.

Figure 3
Return spot from M1, focused on the CCD chip. (a)–(c) Correction of the vertical error. (d)–(e) Shrinking of the line profile into a spot by gradual correction of the horizontal error.

3.2. Alignment of the interferometer to mirror M1

In order to bring the source point of the LUPI close enough to the focus of mirror M1 and to obtain a visually resolvable interference pattern which then could be further corrected, a prealignment step is needed (http://www.sorl.com; Barkhouser & Ohl IV, 1999). For this purpose, a glass retro-reflector prism (surface quality $\lambda/10$) was placed behind M1 at a distance of approximately 10 cm (Fig. 2, point C). The beam in the reference arm was blocked and an imaging lens was put into the test arm in front of the CCD camera such that the camera is at the focus of the lens (Fig. 2, point A). This allowed the observation of the return spot from the test arm, focused on the CCD (see Fig. 3). The goal of this pre-alignment step was to achieve the best possible focusing of the return spot. As a retro-reflector always provides back-reflection, only adjustments of the hexapod in X, Y and Z coordinates were needed. The initially obtained shape of the return spot was a skewed line. Vertical adjustment of the hexapod [Figs. 3(a)–3(c)] corrected the angle of the line towards the horizontal, thus removing the XY component of the observed astigmatism. Continuous horizontal adjustment [Figs. 3(d)–3(f)] allowed focusing of the return beam to the smallest possible round-shaped spot, meaning that this pre-alignment step is complete. After finishing the pre-alignment, the retro-reflectror was replaced with the high-quality optical flat mirror, the imaging lens was removed and the beam in the reference arm was unblocked, thus revealing an interference pattern on the CCD chip. Fu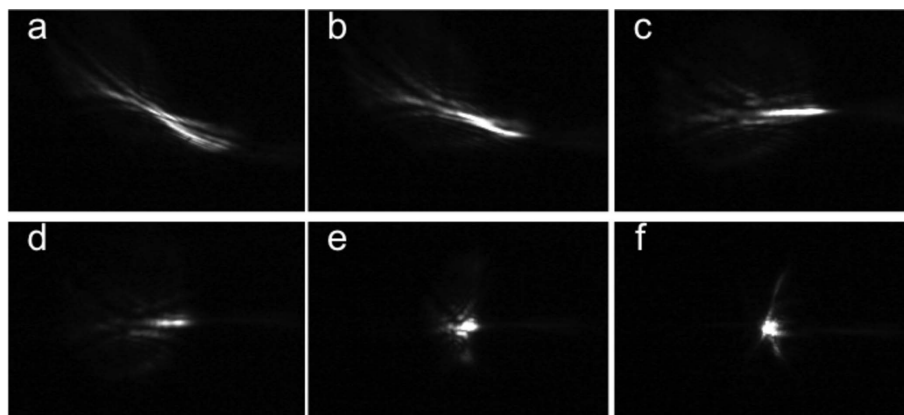rther and therefore more precise alignment is achieved by adjusting the horizontal/vertical position of the source point followed by a tip/tilt correction of the OF.

A sequence of interferograms showing progressive vertical and horizontal alignment is presented in Fig. 4. The obtained pattern is cross-like with an additional tilt, indicating both $Y2$–$X2$ and XY astigmatism, according to Zernike theory (Born & Wolf, 1965). Such a pattern appears due to an incorrect height and off-axis distance (OAD) of the source point with respect to the mirror M1. The correction of the vertical offset [Figs. 4(a)–4(c)] results in a gradual rotation of the 'cross' such that it is symmetric with respect to the center horizontal and vertical lines. This adjustment removes the XY components of the astigmatic aberration. As soon as this is achieved, the OAD needs to be corrected. A shift of the source into the correct direction results in the enlargement of the cross and finally in its transformation into a set of concentric circles [Figs. 4(d)–4(f)]. The next alignment step is adjusting the
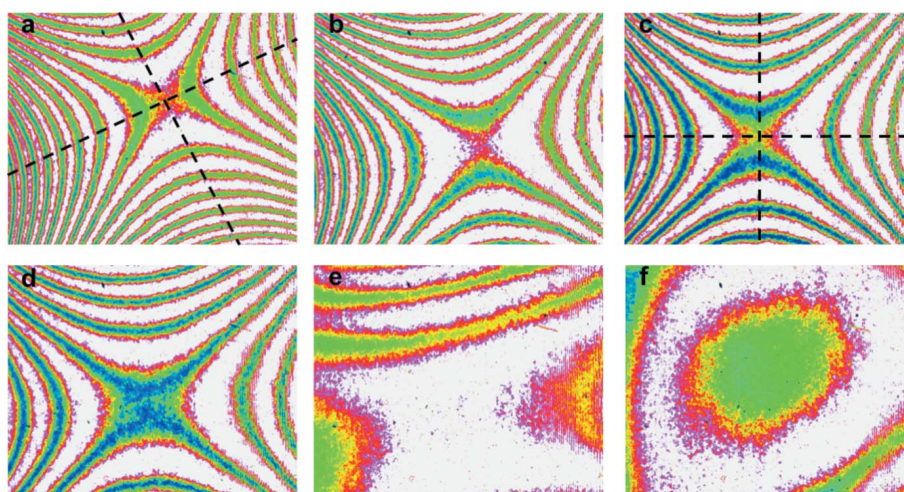

Figure 4
Interferograms showing the alignment of the LUPI to the M1 mirror. OF was used to provide back-reflection on M1. (a)–(c) Progressive vertical alignment leads to the rotation of the astigmatic 'cross' pattern. (d)–(f) Good vertical and progressive horizontal alignment. Some residual vertical misalignment becomes visible in image (f).
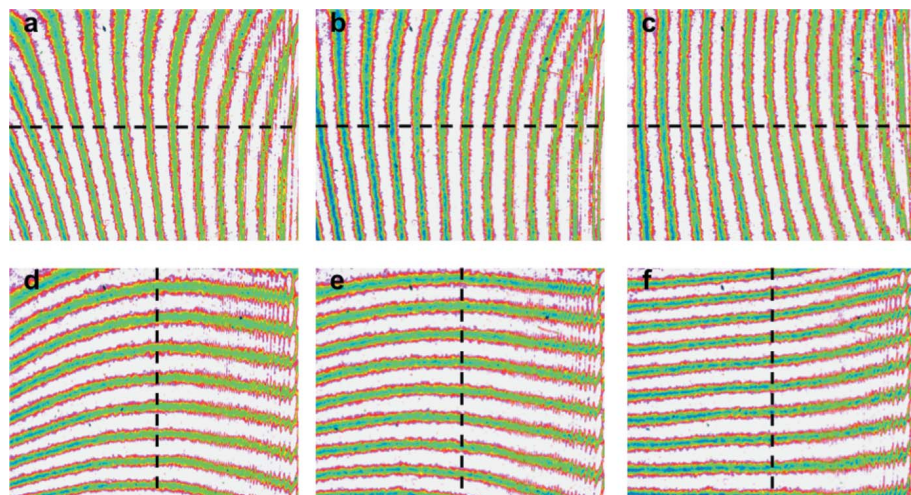
Figure 5
Introduction of a tilt into the system for visualization of the residual aberrations and their consequent correction. (*a*)–(*c*) Correction of the vertical error. (*e*)–(*f*) Correction of the horizontal error. Panels (*c*) and (*f*) show the final interference patterns.

source to the correct focal distance. Again, a shift in the correct direction along the M1 optical axis enlarges the circles and increases the period of the interference pattern.

Finally, a uniform intensity distribution (piston) can theoretically be achieved, meaning that two plane parallel waves interfere. Vibrations in the experimental hall and air turbulences can obscure the interference pattern and residual aberrations, which makes further improvements challenging; in particular, when the source point is very close to the M1 focus and the observed fringes period is such that not more than 1–2 fringes are visible. Therefore, after obtaining a piston-like pattern, a tilt was introduced to the system deliberately. This was achieved by tipping/tilting the reference flat to observe 5–7 horizontal and vertical lines in the pattern, respectively. The goal was to make them symmetric around the imaginary line that goes through the center of the interference pattern, perpendicular to the fringes (see Fig. 5). This would mean that the reflected wavefront in the reference arm is flat and the source point is at the focus of M1.

First, the reference flat mirror of the LUPI was tilted to obtain vertical lines in the pattern. The vertical position of the source point was adjusted together with the tip of the OF to achieve the required symmetry condition [Figs. 5(*a*)–5(*c*)]. After that, the reference flat was adjusted to observe horizontal fringes. The OAD of the source point and tilt of the OF were optimized to form parallel and straight fringes [Figs. 5(*e*)–5(*f*)]. Figs. 5(*c*) and 5(*f*) show the final optimized patterns.

After having aligned the LUPI system to M1, the optical flat mirror was removed and the spectrometer grating bench was rotated into a 90° configuration perpendicular to the optical axis of M1, in order to provide back-reflec-

tion of the collimated light on M1. This configuration allowed aligning all gratings installed to have identical interference patterns. This ensures that the imaging properties of the spectrometer as well as its resolution will not depend on the grating that is being used. The obtained interferograms of the installed gratings and the mirror blank are compared in Fig. 6.

3.3. Alignment of the mirror M2

After having aligned the LUPI–M1 gratings systems, the grating bench was returned to its nominal zeroth-order diffraction position of 9° relative to the optical axis of M1, and the OF was placed on a high-precision translation stage at the focus of the parabolic mirror M2 (see Fig. 2, point D). The interference pattern showed the presence of both Y^2–X^2 and XY astigmatism contributions. The latter could be corrected by changing either the pitch of the grating bench or the yaw angle of the mirror M2. The correction of the XY astigmatism was achieved by small adjustment of the zeroth-order angle of the grating bench by less than 2 mrad.

In order to obtain a full quantitative analysis of the remaining aberrations we switched from interference pattern measurements to wavefront sensor measurements. A direct measurement of the wavefront eliminates the issue of low contrast in the interference pattern due to intensity attenuation of the light in the test arm of the LUPI, compared with its reference arm. The reason for the low intensity is simply because of six additional reflections from M1–blank-mirror–M2 upon forward and backward light propagation, considering that the mirror diamond-like carbon coating is optimized for XUV photons.

Wavefront measurements were carried out using a Hartmann–Shack wavefront sensor from Laser-Laboratorium Göttingen eV (LOT). It is sensitive in the wavelength range 350–1100 nm and consists of a 12 mm × 12 mm microlens array in a focal distance of 3.6 mm to the CCD camera. The
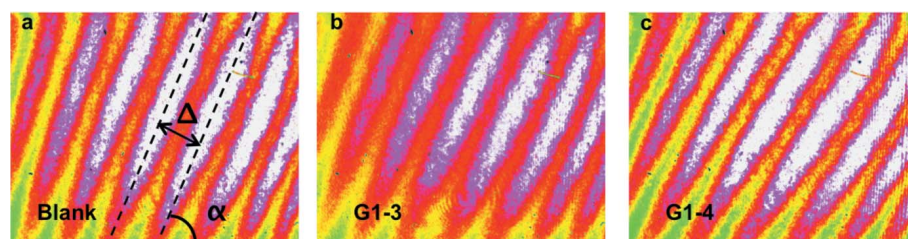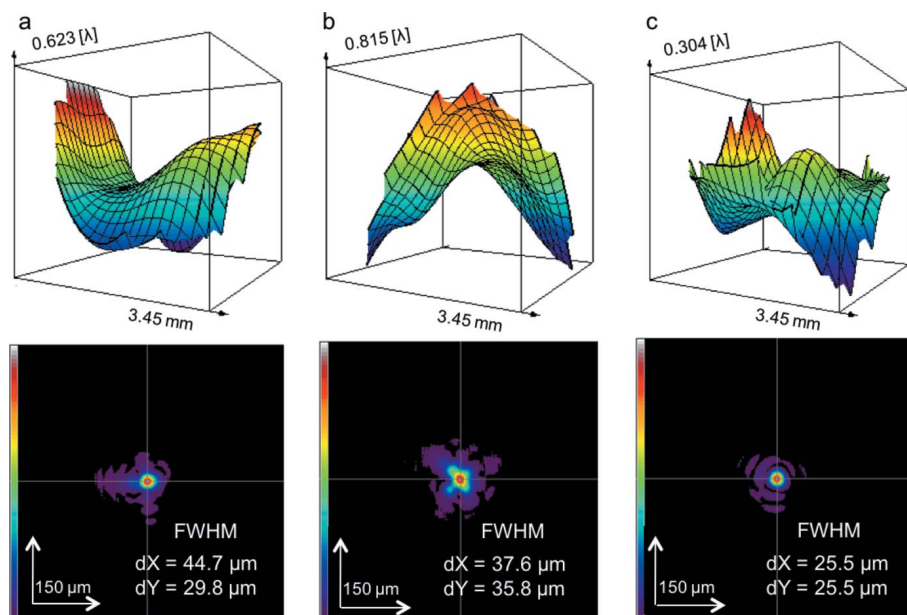

Figure 6
Tilt fringes showing resulting alignment of the blank mirror (*a*) and the installed diffraction gratings (*b*) and (*c*). The patterns are obtained by placing the above-mentioned optical elements (diffraction gratings, blank mirror) in the 90° orientation, to provide back-reflection on M1. The identical tilt of the fringes and their equal periods confirm their proper alignment with respect to each other and to the mirror M1.

Figure 7
In the upper row, measured wavefronts behind the mirror M2 are shown at the position of the wavefront sensor. The inital wavefront shows a dominant presence of astigmatic contributions (a), wavefront after pitch optimization of M2 (b) and the final wavefront after alignment of roll and x of M2 (c). The peak-to-valley value for each wavefront is given in λ and could be reduced to about half of the initial value. The lower row shows the intensity profiles at the focus position of M2. They were retrieved by Fresnel back-propagation of the intensity profile measured at the position of the wavefront sensor. The focus size in the x and y direction is given as the FWHM for the cross-marked positions. The focus size could be significantly reduced to a circular shape of about 25.5 μm each in the x and y directions.

Table 1
Zernike aberrations, corresponding to the wavefronts in Fig. 7 for λ = 633 nm.

Zernike aberrations	(a)	(b)	(c)
Astigmatism Y^2–X^2	0.237λ	0.115λ	0.021λ
Astigmatism XY	0.079λ	0.375λ	0.002λ
Coma X	0.109λ	0.071λ	0.077λ
Coma Y	0.009λ	0.032λ	0.000λ
Triangular coma	0.051λ	0.019λ	0.049λ
Quadratic astigmatism	0.008λ	0.038λ	0.017λ
Spherical aberration	0.008λ	0.046λ	0.016λ

lenses are 150 μm × 150 μm in size. The 12 bit CCD camera has a resolution of 1280 × 1040 pixels with a field of view of 8.25 mm (h) × 6.6 mm (v). The absolute accuracy at 633 nm is between λ/50 and λ/150, with a relative sensitivity up to λ/10000.

Wavefronts showing the alignment procedure of the M2 mirror together with the focal spots retrieved by Fresnel back-propagation of the measured intensity distribution are presented in Fig. 7. The first Zernike aberrations for each wavefront were calculated using the Arizona-Fringe notation with 37 polynomials and are summarized in Table 1 (Laser Beam Profiler MrBeam, Version 3.7.0, Laser-Laboratorium-Göttingen, Germany).

In the upper row in Fig. 7 the measured wavefronts behind the mirror M2 are shown at the position of the wavefront sensor which was installed ∼30 cm behind the focus position

of M2. In Fig. 7(a) the initial wavefront behind the mirror M2 prior to correction of the zeroth-order angle of the grating bench is dominated by the Y^2–X^2 astigmatic contribution, in agreement with the interferometric measurements. Optimization of the M2 pitch angle corrects the Y^2–X^2 component of the astigmatism [Fig. 7(b)], leaving the XY one. Finally, correction of roll and x of the M2 mirror eliminates the remaining aberrations and yields to the final wavefront, shown in Fig. 7(c). The peak-to-valley value for each wavefront is given in λ and could be reduced to about half of the initial value. The size of the focus could significantly be reduced to a circular shape of about 25.5 μm each in the x and y directions.

After completion of the M2 alignment, OF was returned to the focus of M2 and the gratings bench was scanned, yielding final interference patterns of the aligned SP1 optical elements (Fig. 8) with different gratings of the monochromator chamber, installed in the beam and confirming proper alignment of the system. The best straightness and parallel nature of the interference pattern can be obtained for the blank and grating G1-3, whereas G1-4 shows a slightly increased tilting of the interference fringes.

4. Offline X-ray measurements

After completion of the interferometric alignment with visible photons, the performance of the spectrometer was characterized in the soft X-ray range utilizing a Manson model X-ray source (McPherson light source, model 642), depicted in Fig. 9. The source is equipped with a 200 μm pinhole rigidly mounted in front of the photon-emitting anode at a distance of 16 mm (see Fig. 9). For spectrometer performance characterization, the Al $L_{2,3}$ emission line of the Al–Mn anode was investigated. The chamber with the X-ray tube was mounted on the hexapod instead of the LUPI interferometer and the pinhole was brought to the M1 focus. Both the Manson source pinhole and the LUPI pinhole were fiducialized in advance. The replacement of the LUPI with Manson's source was performed under surveying with approximately 300 μm precision. The wavefront sensor (Fig. 1) was replaced by an ICCD camera from Princeton Instruments (PIXIS-XO 2048B), attached to the spectrometer chamber via the metal bellows and placed in the nominal focal position. The mounting platform below the ICCD camera is motorized and allows the camera to be moved along the optical axis of M2. The entire system consisting of the monochromator and the ICCD camera acts like a one-stage spectrometer. A 3D scan of
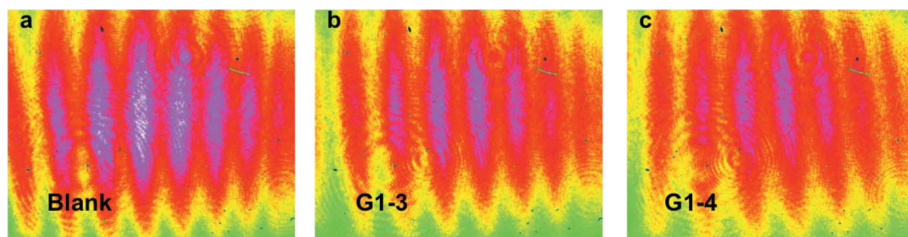
Figure 8
Interference fringes showing the final alignment of the blank mirror (*a*) and diffraction gratings (*b*), (*c*). The patterns were obtained after M2 alignment with OF placed at the M2 focus. The identical tilt of the fringes and their equal periods indicate interference of two plane waves, thus confirming proper alignment of the optical elements with respect to each other as well as to the mirrors M1 and M2.
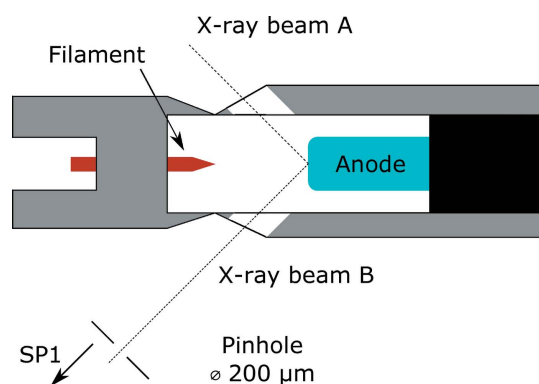

Figure 9
Schematic drawing of the X-ray source used in verification of the spectrometer performance. The pinhole is located 16 mm away from the anodes surface.

the source position combined with a longitudinal scan of the ICCD position was performed with the spectrometer in the zeroth order (imaging mode) to bring the X-ray source exactly to the M1 focus with an accuracy of 50 μm. An optimized pinhole image was obtained at the position of the ICCD camera $x_0 = 125$ mm in our coordinate system.

The spectrometer performance in the soft X-ray range was tested in terms of imaging properties in the zeroth diffraction order, in terms of spectrally resolving properties in the first and second diffraction orders, as well as simulations carried out for comparison. These verification steps will be discussed in more detail in the following sections.

4.1. Comparison of the *SHADOW* simulations with X-ray source experiment

Prior to performing the alignment procedure and experimental studies with the Manson source, the first monochromator stage and the source have been extensively studied in terms of possible effects of optics and source point misalignments via ray tracing using the *SHADOW* software package (Cerrina & Sanches del Rio, 2010).

The source for the ray tracing has a uniform photon energy distribution from 73.1 eV to 61.1 eV to mimic the 12 eV energy width of the Al $L_{2,3}$ emission line (Neddermeyer & Wiech, 1970; Ederer *et al.*, 1988; Poletto *et al.*, 1999), circular

shape with radius of 0.3 mm, and a uniform divergence of 14 mrad FWHM.

Specifications and slope errors of the optical elements of the first monochromator used for the ray tracing have been given by Dziarzhytski *et al.* (2018). Here, the only difference is that an additional circular pinhole with 0.1 mm radius is placed at a distance of 550 mm in front of the first parabolic mirror M1, *i.e.* at its focus. The source is placed at the distance of 566 mm from the mirror M1, which corresponds to the actual distance of 16 mm between the anode surface and the limiting pinhole.
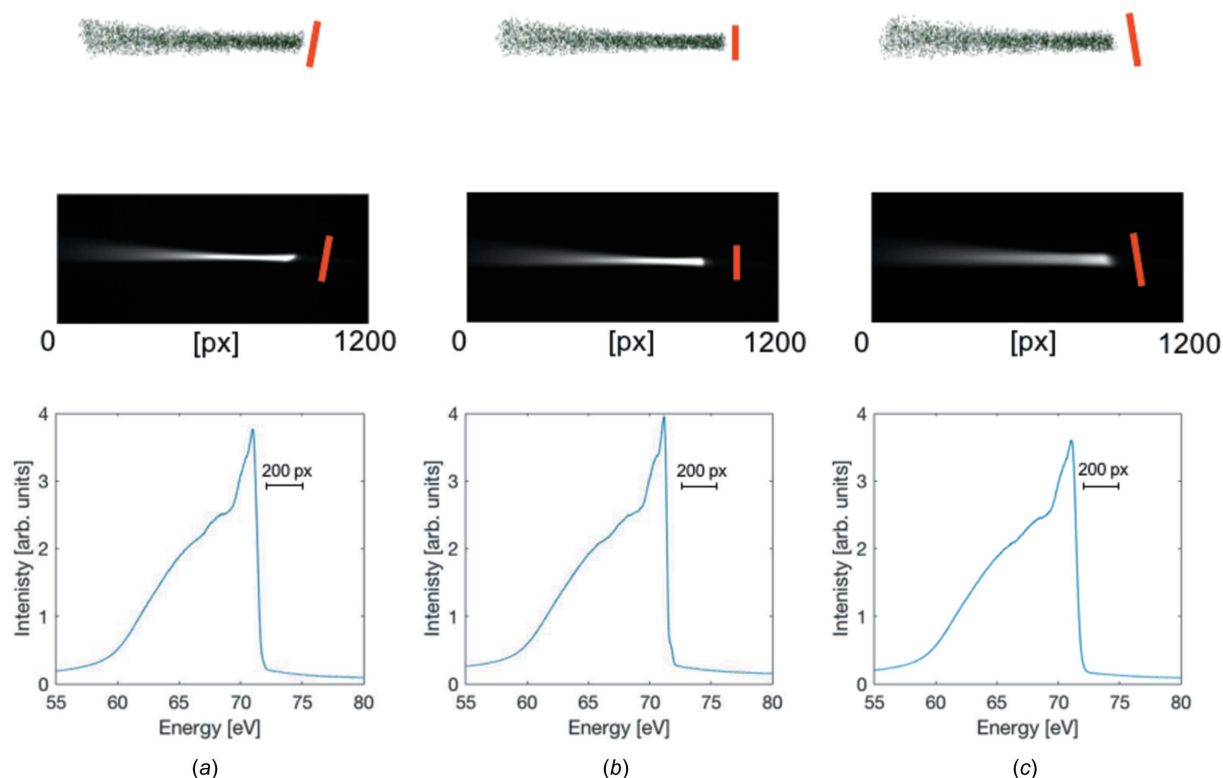
As discussed in Section 2, the spectrometer disperses the collected light in the vertical plane, therefore the vertical source size and its spectral bandwidth defines the spectral resolution of the spectrometer to a large extent. The calculated highest spectral resolution of the spectrometer at 73 eV photon energy, presuming a vertical source size of 200 μm, is 220 meV for the grating G1-3 (576 l mm^{-1} groove density) and 90 meV for G1-4 (1120 l mm^{-1} groove density), both working in the first diffraction order. The resolution of the spectrometer with the G1-3 grating in the second diffraction order at the same photon energy is 85 meV.

Ray-tracing results for the spectrometer imaging properties in the first diffraction order along the beam caustic in comparison with experimentally recorded images of the pinhole are shown in Fig. 10. The detector plane has been shifted upstream and downstream by 35 mm relative to the nominal focal position [see Figs. 10(*a*)–10(*c*)]. A change of the slope of the high-energy flank (right side) along the caustic is observed in both simulations and experiment. The line is added as a guide for the eye in the figures. Such a change of the flank leads to a decrease of the spectrometer resolution due to smearing out the sharp L_3 rising edge and L_2 peak while binning. This criterion was used in the measurements with the X-ray tube to define the focal position of the SP1 monochromator unit.
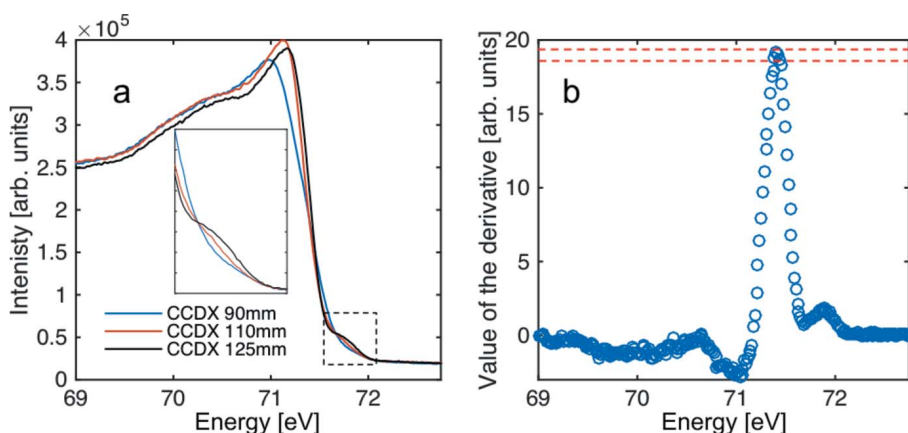
4.2. Determination of the focal position

Aberrations lead to the distortion of the image in the first order, resulting in a decrease of the slope of the rising edge of the Al L_3 emission peak and smearing out the splitting resulting from the spin–orbit coupling, thus providing a good criterion for the position of the focal plane of the spectrometer and its resolution. This criterion is especially applicable, because the Al L_3 edge has a sharp rising edge near the Fermi energy E_f, which is mostly broadened due to the instrument response function (Neddermeyer & Wiech, 1970; Ederer *et al.*, 1988; Poletto *et al.*, 1999). The longitudinal position of the ICCD camera was scanned within the ±35 mm range from the position where the best zeroth-order image was found. The recorded spectral intensity distribution at each detector position was background-corrected and integrated within the

Figure 10
Simulated (top row) and measured (middle row) 2D images of the Al $L_{2,3}$ band as well as projected intensity profiles (bottom) for different longitudinal positions of the detector: −35 mm from the nominal focus (*a*), at focus (*b*) and +35 mm from the focus (*c*). A change of the slope of the high-energy flank (right side) along the caustic is observed in both simulations and experiment. The line is added as a guide to the eye. Energy is increasing from left to right.

region of interest, yielding the Al $L_{2,3}$ X-ray fluorescence spectrum (Fig. 10, bottom). The slope of the rising edge of each spectrum was calculated as the average of the five highest values of the first derivative of the measured spectrum in the vicinity of the rising edge [see Figs. 11(*a*) and 11(*b*)]. Error bars were extracted as a standard deviation for these five points. Slope dependencies for each grating were normalized to 1. Measurements were performed for grating G1-3 in the first and second diffraction orders, mimicking different photon energies, and for G1-4 in the first diffraction order. Results of the analysis are presented in Fig. 12, and are summarized in Table 2. As one can see, the maxima for all scans are within the range 123.2–125.3 mm, whereas the optimum zeroth-order image was found to be at 125 mm. This confirms that the position of the focal plane for both gratings does not change within the measurement precision when going from the zeroth diffraction order to 73 eV for the G1-4 grating and 73 eV and 36.5 eV energies for the G1-3 grating. This ensures that the spectrum after the first monochromator stage will always be projected onto the fixed intermediate slit plane, most efficiently suppressing the stray light and coupling the desired energy window correctly into the second monochromator.

A zoom of the rising-edge region of the Al $L_{2,3}$ spectrum, confirming the improvement of the resolution and formation of the L_2 pre-edge (inset)

Figure 11
(*a*) Formation of the pre-edge feature at 71.8 eV and decrease in the slope of the rising edge of the Al $L_{2,3}$ spectrum upon approaching to the CCDX = 125 mm position. (*b*) Example of the derivative used for the slope analysis (first derivative of the spectrum, measured with the G1-3 grating in the first diffraction order at CCDX = 125 mm). Red lines indicate the borders of the range, within which the average value of the derivative and the error bar are calculated.
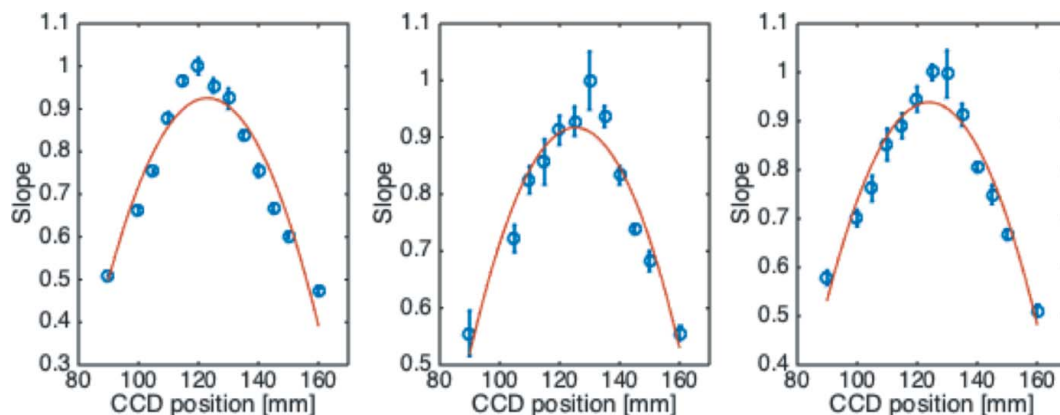
Figure 12
Increase in the slope of the rising edge of the Al $L_{2,3}$ X-ray fluorescence spectrum for the G1-3 grating in the first order (left), G1-3 in the second diffraction order (middle) and G1-4 in the first diffraction order (right) upon approach of the CCD position to 125 mm. The red line is the fit of the parabolic function to the data.

Table 2
Positions of the maximum of the parabolic fit with 90% confidence band to the experimentally measured dependencies of the slope of the rising edge of Al $L_{2,3}$ X-ray fluorescence.

The optimum zeroth-order position is at 125.0 mm.

G1-3 first order	G1-3 second order	G1-4 first order
123.2 ± 3.2 mm	125.3 ± 3.5 mm	123.9 ± 3 mm

Table 3
Comparison of the spectrometer resolution measured with Manson's source and calculated using *SHADOW*.

Grating	G1-3	G1-3	G1-4
Photon energy	73 eV	36.5 eV	73 eV
Experiment	239 ± 24 meV	102 ± 10.2 meV	200 ± 20 meV
Theory	220 meV	85 meV	90 meV

upon correction of the ICCD longitudinal position, is presented in Fig. 11(*a*).

Estimated widths of the L_3 edge as a measure of the spectrometer resolution recorded with different gratings and diffraction orders are compared with theoretical ones as obtained in the ray tracing and are summarized in Table 3. This table shows that for grating G1-3 both first- and second-order resolutions as determined by our experiments match the ray-tracing results within the experimental resolution. Grating G1-4, however, which should show a similar resolution as G1-3 in the second-order, exhibits a performance which is about a factor of two off. This might be connected to a number of factors indicating a poorer quality of G1-4 such as grating inhomogeneities, which are difficult to address through a ray-tracing simulation. Furthermore, as already discussed for Fig. 8, the interferences fringes in Fig. 8(*c*) do not show the same quality of the straightness and are not as parallel to each other as compared with grating G1-3. Together this can result very well in the reduced resolution of grating G1-4.

5. Conclusions

In this work an advanced alignment concept was applied to the XUV Raman monochromator. Optical laser interferometry measurements together with wavefront measurements were used to align the monochromator. Both methods qualitatively and quantitatively verify the alignment. The aligned state of the instrument was further confirmed in the XUV energy range by investigating the X-ray fluorescence at the Al $L_{2,3}$ edge with the help of an off-line X-ray source compared with

SHADOW ray-tracing results. Taking into account that the investigated effective energy range covers almost the entire working range of grating G1-3 and the identical interferometric alignment of both gratings, we can conclude that the spectrometer performs within its design specifications.

References

Ackermann, W. *et al.* (2007). *Nat. Photon.* **1**, 336–342.
Ament, L. J. P., van Veenendaal, M., Devereaux, T. P., Hill, J. P. & van den Brink, J. (2011). *Rev. Mod. Phys.* **83**, 705–767.
Barkhouser, R. H. & Ohl IV, R. G. (1999). *Proc. SPIE*, **3782**, 601–614.
Born, M. & Wolf, E. (1965). *Principles of Optics*, Section 9.2. New York: Pergamon.
Cerrina, F. & Sanches del Rio, M. (2010). *Handbook of Optics*, 3rd ed., ch. 35. New York: McGraw Hill.
Dziarzhytski, S., Gerasimova, N., Goderich, R., Mey, T., Reininger, R., Rübhausen, M., Siewert, F., Weigelt, H. & Brenner, G. (2016). *J Synchrotron Rad.* **23**, 123–131.

Dziarzhytski, S., Siewert, F., Sokolov, A., Gwalt, G., Seliger, T., Rübhausen, M., Weigelt, H. & Brenner, G. (2018). *J. Synchrotron Rad.* **25**, 138–144.

Ederer, D. L., Schaefer, R., Tsang, K., Zhang, C. H., Callcott, T. A. & Arakawa, E. T. (1988). *Phys. Rev. B*, **37**, 8594–8597.

Keitel, B., Plönjes, E., Kreis, S., Kuhlmann, M., Tiedtke, K., Mey, T., Schäfer, B. & Mann, K. (2016). *J. Synchrotron Rad.* **23**, 43–49.

Kotani, A. & Shin, S. (2001). *Rev. Mod. Phys.* **73**, 203.

Martins, M., Wellhöfer, M., Hoeft, J. T., Wurth, W., Feldhaus, J. & Follath, R. (2006). *Rev. Sci. Instrum.* **77**, 115108.

Neddermeyer, H. & Wiech, G. (1970). *Phys. Lett. A*, **31**, 17–18.

Poletto, L., Boscolo, A. & Tondello, G. (1999). *Proc. SPIE*, **3764**, 94–102.

Rübhausen, M., Schulz, B., Burth, K., Bäckström, J., Kunze, J., Reininger, R., Nordgren, J., Söderström, J., Rubensson, J.-E., Börjesson, L., Abbamonte, P., Cooper, S. L., Martins, M., Föhlisch, A., Wurth, W., Feldhaus, J. & Schneider, J. (2004). Technical Design Report. BMBF Project No. 05KS4GU2. DESY, Hamburg, Germany.

Rusydi, A., Goos, A., Binder, S., Eich, A., Botril, K., Abbamonte, P., Yu, X., Breese, M., Eisaki, H., Fujimaki, Y., Uchida, S., Guerassimova, N., Treusch, R., Feldhaus, J., Reininger, R., Klein, M. & Rübhausen, M. (2014). *Phys. Rev. Lett.* **113**, 067001.

Schäfer, B., Lübbecke, M. & Mann, K. (2006). *Rev. Sci. Instrum.* **77**, 053103.

Tiedke, K. *et al.* (2009). *New J. Phys.* **11**, 023029.